



## Research paper

# Band alignment and charge transfer pathway in three phase anatase-rutile-brookite TiO<sub>2</sub> nanotubes: An efficient photocatalyst for water splitting



L.K. Preethi<sup>a,\*</sup>, Tom Mathews<sup>a,\*</sup>, Mangla Nand<sup>b</sup>, S.N. Jha<sup>b</sup>, Chinnakonda S. Gopinath<sup>c</sup>, S. Dash<sup>a</sup>

<sup>a</sup> Surface and Nanoscience Division, Materials Science Group, Indira Gandhi Centre for Atomic Research, HBNI, Kalpakkam 603 102, India

<sup>b</sup> Atomic and Molecular Physics Division, Bhabha Atomic Research Centre, Mumbai 400 085, India

<sup>c</sup> Catalysis Division, National Chemical Laboratory, Dr. Homi Bhabha Road, Pune 411 008, India

## ARTICLE INFO

## Article history:

Received 7 November 2016

Received in revised form 1 June 2017

Accepted 12 June 2017

Available online 17 June 2017

## Keywords:

Anatase-rutile-brookite

Photocatalysis

Photoluminescence

Valence band edge

Hydrogen generation

Nanotubes

## ABSTRACT

The study reports electrochemical synthesis, phase evolution and hydrogen generation efficiency of anatase, anatase-rutile and anatase-rutile-brookite (ARB) TiO<sub>2</sub> nanotubes for the first time. The SEM and TEM micrographs confirm the tubular morphology of the samples. The presence of anatase, rutile and brookite phases in a single nanotube is confirmed from high resolution TEM analysis. The water splitting efficiency of the three systems are studied under one sun illumination. It is observed that the anatase-rutile-brookite TiO<sub>2</sub> nanotubes are highly efficient compared to anatase-rutile or anatase TiO<sub>2</sub> nanotubes. The hydrogen generated by ARB composites, after four hours of one sun illumination, is found to be nearly twice that of anatase TiO<sub>2</sub> nanotubes and 1.6 times that of anatase-rutile TiO<sub>2</sub> nanotubes. The results suggest that the ARB in single nanotube having two junction interfaces, highly facilitate inter-particle charge transfer compared to single junction anatase-rutile or bare anatase TiO<sub>2</sub> nanotubes. From the deconvolution of PL spectra and the synchrotron radiation assisted valence band edge analysis, the band diagram for the anatase-rutile-brookite phase is constructed. The charge separation and its transfer pathway for efficient photo-assisted water splitting are delineated. This opens a new route for the simple synthesis and study of tri-phase TiO<sub>2</sub> for efficient photocatalytic water splitting compared to the widely studied two phase TiO<sub>2</sub>.

© 2017 Published by Elsevier B.V.

## 1. Introduction

Hydrogen is identified as a potential fuel of future because of its high energy density and environmental friendly nature [1,2]. Among the techniques used to generate hydrogen, photocatalytic water splitting is highly desirable due to low carbon emission and the utilization of abundant natural resources such as water and sunlight [3,4]. Since the pioneering work of Fujishima and Honda [3], many materials such as oxides [5], nitrides [6], and sulphides [7], have been studied for water splitting. Among them, TiO<sub>2</sub>, whose band edges suitably aligned with water redox potentials is best suitable for water splitting due to its stable, inexpensive and non-corrosive nature. Even though the water splitting efficiency of TiO<sub>2</sub> is attributed to its energy band characteristics, the physical and

chemical properties of TiO<sub>2</sub> are sensitive to the phase composition. TiO<sub>2</sub> has three different crystalline forms viz anatase, rutile and brookite, among which anatase shows the highest photocatalytic performances [8–10]. The high photocatalytic efficiency of anatase is due to its prolonged lifetime of charge carriers and spatial charge separation [11]. However the photocatalytic activity of TiO<sub>2</sub> is strongly limited by its low quantum efficiency due to fast recombination of excited electron-hole pairs [12]. It has been demonstrated that the effective strategy to inhibit the recombination is to introduce the phase junctions in TiO<sub>2</sub> catalyst [11]. Recent studies have reported that anatase TiO<sub>2</sub> having some fraction of rutile phase shows enhanced photocatalytic activity compared to pure anatase due to the efficient charge separation by the band edge alignment at the anatase/rutile interface [11–13]. There are also reports on studies of anatase/brookite [14,15] and brookite/rutile phase interfaces [16], which perform well in photocatalytic application compared to individual phases. There are few recent reports on the synthesis of anatase/rutile/brookite (ARB) triphase TiO<sub>2</sub> and its photocatalytic application [17–19]. Although ARB is a rare polymorph and its syn-

\* Corresponding authors.

E-mail addresses: [preaag@gmail.com](mailto:preaag@gmail.com) (L.K. Preethi), [tom@igcar.gov.in](mailto:tom@igcar.gov.in) (T. Mathews).

thesis involves multiple steps of rigorous reactions and/thermal treatment, their importance in photocatalysis is recently realized [20–22]. The phase selection in these synthesis techniques depends on the reactant concentration, temperature and reaction time [22–24]. Moreover the triphase obtained by most of these synthesis methods can be easily separated by peptization to individual phase  $\text{TiO}_2$  nanoparticles where the efficiency of triphase interface is doubted due to the dispersive nature of the colloids [18,19,24]. Similarly, unlike anatase-rutile biphasic system, studies on electron transfer pathway mechanism in ARB triphase system has not yet come to the spotlight to determine the underlying physics behind the high efficiency of the systems.

Unlike the widely studied anatase or anatase/rutile systems, the reports on water splitting efficiency of ARB triphase  $\text{TiO}_2$  nanostructures is unavailable to the best of author's knowledge. To understand the actual reactivity of triphase  $\text{TiO}_2$  nanostructures in the photocatalytic water splitting, a facile synthesis of  $\text{TiO}_2$  nanoparticles having three phases in single entity whose phase compositions are not separated by dispersion, as well as a clear cut picture of the charge transfer mechanism in triphase system is highly appreciable.

Herein, we report a novel and simple synthesis technique to prepare triphase  $\text{TiO}_2$  nanotube powders which does not require the use of expensive, time consuming thermal or hydrothermal or rigorous acidic treatments. The anatase, anatase-rutile and anatase-rutile-brookite  $\text{TiO}_2$  nanotube powders were obtained by tuning the potential in electrochemical anodization technique. Unlike in other experimental techniques, all the three phases of  $\text{TiO}_2$  are obtained in a single nanotube. The phase transition behavior with respect to applied voltage is studied. The obtained nanotube powders are used in photocatalytic water splitting experiments to compare the efficiency of single, double and triphase  $\text{TiO}_2$  nanotubes. For the first time, a band diagram is proposed for ARB system with the possible electron transfer pathway.

## 2. Experimental

### 2.1. Synthesis of $\text{TiO}_2$ nanotube powders

$\text{TiO}_2$  nanotube powders are synthesized by, previously reported, potentiostatic rapid breakdown anodization technique using titanium and platinum foils as the working and counter electrodes, respectively, in 0.1 M perchloric acid electrolyte [25]. Before performing the experiment, the titanium foil (0.5 mm thickness, 99% pure, cut to the size of area  $2.5 \times 0.5 \text{ cm}^2$ ) is polished smoothly to remove the oxide layer on the surface. The polished foils are ultrasonicated in alcohol, acetone followed by water and dried in  $\text{N}_2$  gas stream. A constant potential is applied across the electrodes (Pt mesh and Ti foil), kept 15 mm apart in 0.1 M  $\text{HClO}_4$ , using a programmable DC power supply (Agilent N6700series). The synthesis is done at various voltages viz 9.5, 10.2, 11, 12 and 15, where 9.5 V is the threshold voltage for the rapid breakdown anodization (below which no  $\text{TiO}_2$  nanopowders are seen to fall into the solution) to occur.

The anodization process is continued till the whole titanium foil is etched into  $\text{TiO}_2$  powders. The  $\text{TiO}_2$  powders obtained are washed several times with de-ionized water, centrifuged and dried at  $70^\circ\text{C}$  for 15 h. The  $\text{TiO}_2$  powders synthesized at 9.5, 10.2, 11, 12 and 15 V are referred as T-9.5, T-10.2, T-11, T-12 and T-15, respectively, hereafter.

### 2.2. Materials characterization

The morphological analysis of the  $\text{TiO}_2$  nanopowder samples is done by Field Emission Scanning Electron Microscope (FESEM),

(JEOL 6360) and Transmission Electron Microscope (TEM) (JEOL 2010). The samples for TEM studies are prepared by placing a drop of sample suspension in methanol on a carbon coated copper grid and allowing it to dry. The crystal structure of  $\text{TiO}_2$  nanotubes is analyzed by High Resolution TEM (HRTEM). The phase identifications of all the samples are carried out using X-Ray Diffractometer (D8, Bruker). Synchrotron X-ray diffraction measurements were performed using ADXRD beamline on Indus-2 synchrotron source. The beamline consists of adaptive focusing optics and Si(111) based double crystal monochromator. The measurements were performed in transmission mode using Image Plate area detector (Mar 345 dtb) at a wavelength of  $0.82188 \text{ \AA}$ . The rings on Image plate were integrated using Fit2D software to obtain the Intensity vs  $2\theta$  plot. A micro-Raman spectrometer (inVia, Renishaw, UK), in the back scattering configuration, was used with Ar<sup>+</sup> laser (514.5 nm) as excitation source, diffraction gratings of  $1800 \text{ gr mm}^{-1}$  for monochromatization and a thermoelectric cooled charged coupled device (CCD) as detector to study the vibrational modes. An UV Vis spectrometer (PerkinElmer, Lambda 750S) equipped with a 60 mm diameter integrated sphere in reflectance mode is used for band gap measurements. Photoluminescence studies are recorded using a Photoluminescence spectrometer (Renishaw, UK), equipped with a confocal microscope with a “He-Cd laser” operating at 325 nm at a power level of 200 mW.

X-ray photoelectron spectrometer (XPS) (SPECS, Germany) with Al  $\text{K}\alpha$  X-ray source (1486.74 eV) is used for defect analysis. The photoelectron energy spectra were collected using the PHOIBOS 150 MCD-9 analyzer with a resolution of 0.67 eV for 656 kcps at a pass energy of 12 eV. The valence band spectra were measured with angle resolved photoelectron spectroscopy (ARPES) beam line (BL-3) at Indus-1 synchrotron radiation source, RRCAT, Indore. Vacuum in the analysis chamber was better than  $3 \times 10^{-9}$  mbar during the measurements. The analysis chamber is equipped with SPECS PHOIBOS 150 electron analyzer. UPS spectrum from Au foil was used as a reference to characterize the monochromatic synchrotron light from the beamline.

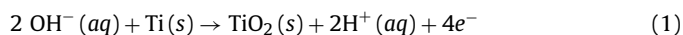
### 2.3. Hydrogen generation studies

The water splitting experiment is carried out by dispersing 10 mg of the photocatalyst in ethanol-aqueous solution (1:4 ratio) in a quartz photocatalytic cell of 50 mL capacity sealed with a rubber septum. The suspension is carefully purged with argon for 30 min. The quartz cell with dispersed sample is kept at 20 cm away from the irradiating solar simulator to ensure one sun conditions (measured irradiation power of Xenon arc lamp is  $300 \text{ mW/cm}^2$  equipped with AM 1.5 cut-off filter). The generated hydrogen is measured every hour by periodically withdrawing gas samples through the rubber septum followed by quantification using a gas chromatograph (GC, Agilent 7690) for the total reaction time of 4 h.

## 3. Results and discussion

### 3.1. Rapid Breakdown anodization (RBA)

The schematic of  $\text{TiO}_2$  nanotube synthesis using RBA technique is shown in Fig. 1a. As soon as we apply a potential difference between the Ti foil and Pt electrode in  $\text{HClO}_4$  solution, the oxide layer grows on the surface of titanium. Below the threshold voltage  $V_t$ , the oxidation of titanium proceeds much more rapidly than that of chlorination by the overall anodic reaction



The applied bias voltage causes an inward migration of oxide ions which increases the oxide layer thickness. At a low anodization

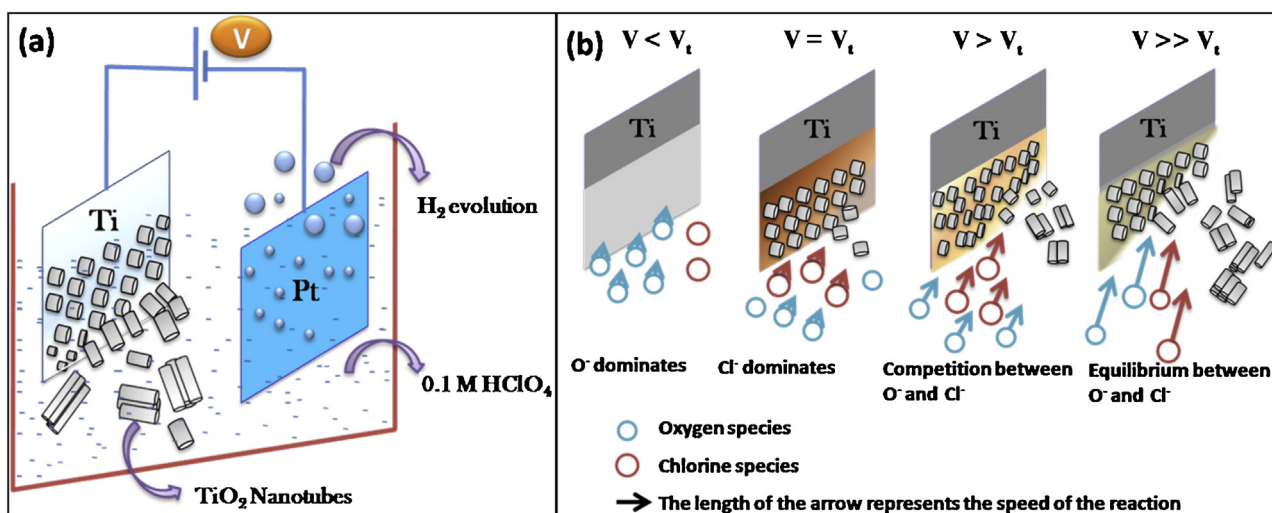


Fig. 1. (a) Schematic representation of synthesis of  $\text{TiO}_2$  nanotubes; (b) A tentative reaction route of the synthesis with respect to voltage.

voltage, the oxidation of titanium dominates that of chlorination even after the formation of a steady state barrier thickness and hence etching of  $\text{TiO}_2$  is not observed. The reaction pathway is schematically depicted in Fig. 1b.

At threshold voltage ( $V_t$ ), the chlorine chemistry begins to compete with the oxygen chemistry causing etching of  $\text{TiO}_2$  layer. This in turn, reduces the oxide thickness and the chlorination interferes with the oxide growth mechanism. At this point, we start to observe the  $\text{TiO}_2$  powders falling out of the Ti foil into the solution. At higher voltages ( $V > V_t$ ), both chlorine chemistry and oxygen chemistry speed up, leading to rapid increase in reaction rates producing more  $\text{TiO}_2$  powders into the solution.

Hence at different voltages there is a rapid change in reaction rates of chlorine species and oxygen species. The earlier reports on RBA technique for the synthesis of nanotubes have concentrated either on the threshold voltage  $V_t$  or the much higher voltages ( $V \gg V_t$ ) [25–27]. However, there are no reports which concentrate on the reactions which occur in between these two extremes where the specific phase growth phenomena take place. Hence in order to study the phase formation with respect to voltage, the anodization were performed at different voltages from 9.5 to 15 V (at 9.5, 10.2, 11, 12 and 15 V) and the  $\text{TiO}_2$  nanotubes obtained are characterized. The synthesis is repeated multiple times and the voltages are constantly monitored to ensure minimum error ( $\pm 0.03$  V) in the set voltage.

### 3.2. The XRD, SEM, TEM and Raman analysis

The XRD pattern of the  $\text{TiO}_2$  powders obtained at different anodization voltages are shown in Fig. 2. From the XRD patterns, it is evident that the nanotubes obtained at 9.5 V (the threshold voltage) are of anatase phase, with a weak residual rutile phase peak around  $54.3^\circ$  and  $69^\circ$ . The XRD pattern of samples synthesized at 10.2 V shows diffraction peaks corresponding to strong anatase and rutile peaks. The two phase formation can be attributed to the competition between chlorination and oxidation at moderate speed. As we increase the synthesis potential to 11 V, the peaks corresponding to brookite are evolved along with anatase and rutile peaks. The phase evolution of rutile and brookite with respect to voltage is shown in the window depicted in Fig. 2. The  $\text{TiO}_2$  powders synthesized at 11 and 12 V have sharp peaks compared to powders synthesized at other voltages. This can be attributed to the good crystallinity of the tri-phase nanotubes resulted from stabilized synthesis voltage at which the equilibrium is reached between oxidation and chlo-

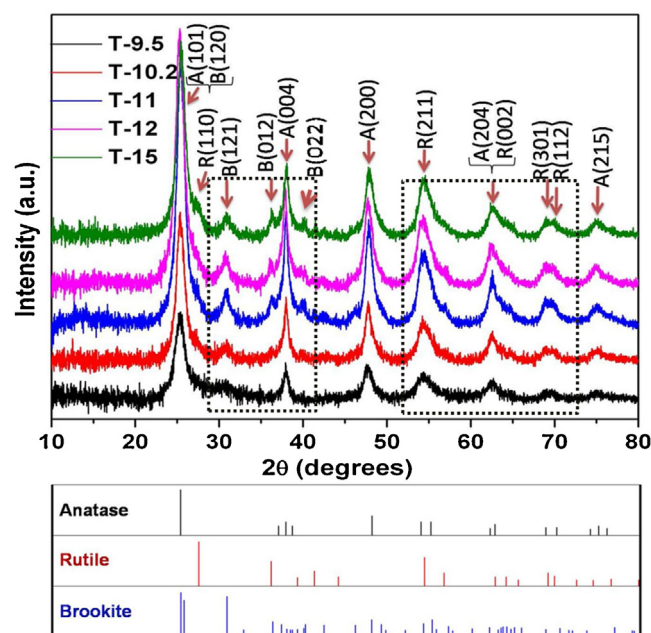


Fig. 2. X-Ray diffraction of  $\text{TiO}_2$  nanotubes synthesized at different voltages.

riation. At higher voltages, the oxidation and chlorination rates are high, which constantly disturbs the phase growth mechanism resulting in non tubular morphology as reflected in T-15 (Fig. 2). The low intensity of the major peak of rutile ( $R(110)$ ) in all the samples can be attributed to the preferred orientation of  $\text{TiO}_2$  nanotubes.

Thus it can be concluded that the phase composition can be changed by simply tuning the DC voltage in RBA technique. The quantification of phases is difficult from the XRD pattern obtained from the lab source (Fig. 2a) due to the poor resolution of rutile (110) peak. Therefore, high resolution synchrotron XRD analysis is carried out for the samples and compared in Fig. 3.

The reflections from the corresponding planes of anatase, rutile and brookite phases are labeled in Fig. 3 after matching the calculated interplanar spacing with that of the one from the JCPDS files (Anatase: 21–1272; Rutile: 21–1276; and Brookite: 29–1360). A clear resolution of the XRD peaks corresponding to reflections from  $R(110)$ ,  $R(111)$ ,  $B(221)$ ,  $R(210)$ ,  $R(301)$  and  $R(112)$  planes is observed, which is poor in case of lab source XRD (Fig. 2). The phase



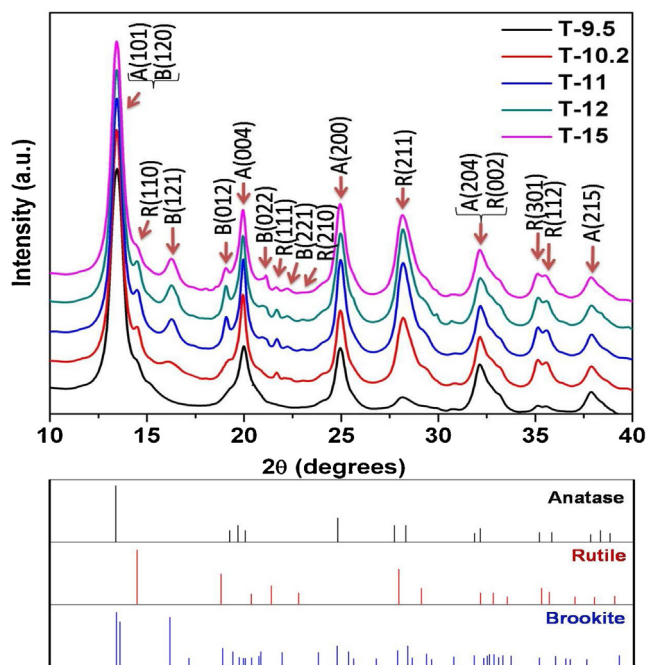


Fig. 3. Synchrotron XRD pattern of  $\text{TiO}_2$  nanotubes synthesized at different voltages.

**Table 1**  
Quantification of phases in  $\text{TiO}_2$  nanotubes synthesized at different voltages.

	Anatase	Rutile	Brookite
T-9.5	94	6	–
T-10.2	67	31	2
T-11	45	26	29
T-12	46	28	26
T-15	44	32	24

evolution with respect to synthesis potential can also be discerned from Fig. 3. The individual phase composition of the samples can be determined using the equations [28]:

$$W_a = KaAa / (KaAa + Ar + KbAb) \quad (2)$$

$$W_r = Ar / (KaAa + Ar + KbAb) \quad (3)$$

$$W_b = KbAb / (KaAa + Ar + KbAb) \quad (4)$$

where  $W_a$ ,  $W_r$  and  $W_b$  represent mass fractions of anatase, rutile and brookite, respectively;  $Aa$ ,  $Ar$  and  $Ab$  represent the integrated intensities of anatase (101), rutile (110) and brookite (121) respectively.  $Ka$  and  $Kb$  stands for correction coefficients whose values are 0.886 and 2.721 respectively [28]. After deconvoluting the overlapping anatase (101) and brookite (120) peaks, calculations are performed using the above formula and the results are listed in Table 1. It is clear that T-9.5 is majorly anatase with residual rutile (6%) and T-10.2 is majorly anatase-rutile with residual brookite (2%).

The tubular morphology of the samples is confirmed from scanning electron micrographs given in Fig. 4. The granular arrangement of particles in tubular orientation is observed in T-9.5 and an improved tubular morphology is observed in T-10.2 sample. This is due to the slow chlorination rate and the large oxide thickness (Fig. 1b). Whereas in T-11 and T-12 samples, the nanotube bundles are clearly seen (Fig. 4c and d). The diameters of the nanotubes in T-11 and T-12 samples are in the range of 30–120 nm. It is evident from Fig. 4e that the tubular morphology of tri-phase  $\text{TiO}_2$  is lost at higher synthesis potential.

TEM images of T-11 are presented in Fig. 5. The bright field images of the nanotubes are shown in Fig. 5a and b. The diameter of

the nanotubes is in the range of 40–120 nm as observed from SEM (Fig. 4). High resolution TEM images of the nanotubes are presented in Fig. 5c and d, with the Fast Fourier Transform (FFT) and Inverse Fast Fourier Transform (IFFT) images of the selected spots on the  $\text{TiO}_2$  nanotube. The images clearly shows the tubular structure of  $\text{TiO}_2$  with the fringes corresponding to anatase (101), brookite (120) and rutile (110). Fig. 5c confirms that all the three phases are present in a single nanotube. The junction observed between different phases of  $\text{TiO}_2$  is an important feature which is expected to allow facile transfer of electrons. This would increase the dispersion of charge carriers and enhance the utilization of charges for redox reactions.

The phase structure of  $\text{TiO}_2$  nanotubes synthesized at different voltages is further examined by Raman spectra analysis (Fig. 6). The characteristic Raman modes of anatase phase around 148, 402, 515, 630  $\text{cm}^{-1}$  are present in all the samples. These peaks are assigned to  $E_g$ ,  $B_{1g}$ ,  $A_{1g}/B_{1g}$  and  $E_g$  modes of anatase phase respectively [25]. The peak corresponding to  $E_g$  mode of rutile appears around 448  $\text{cm}^{-1}$  and is found in all the samples except T-9.5 [29]. A small peak around 240  $\text{cm}^{-1}$ , as a result of second order scattering effect in rutile phase [29], also appears in all the samples except T-9.5. Similarly, the Raman shift corresponding to brookite phase which appears around 245, 322 and 360  $\text{cm}^{-1}$  representing its  $A_{1g}$ ,  $B_{1g}$  and  $B_{2g}$  modes respectively [30] are clearly visible in T-11, T-12 and T-15. Thus Raman studies confirm the phase evolution from anatase to anatase-rutile to anatase-rutile-brookite with increase in synthesis potential.

### 3.3. Band gap analysis of $\text{TiO}_2$ nanotubes having different phase composites

The optical properties of the synthesized  $\text{TiO}_2$  nanotubes were analyzed using UV–vis Diffuse Reflectance Spectroscopy (DRS) (Fig. 7). The Kubelka-Munk (KM) function corresponding to the DRS spectra is denoted as  $F(K)$  which can be written as

$$F(K) = (\alpha h\nu)^{1/n} = A(h\nu - E_g) \quad (5)$$

where  $\alpha$ ,  $\nu$ ,  $A$  and  $E_g$  are absorption coefficient, light frequency, proportionality constant and band gap respectively. The constant value of  $n$  is equal to  $1/2$  or 2, depends on the type of semiconductor. Assuming  $\text{TiO}_2$  as an indirect band gap semiconductor, the band gap can be evaluated from the plot of  $F(K) = (\alpha h\nu)^{1/2}$  vs  $h\nu$ , by extrapolating the straight line to the x-axis. Band gap energies for  $\text{TiO}_2$  nanotubes synthesized at different voltages were found to be around  $3.06 \pm 0.04$  eV. The obtained values are close to the reported values for anatase-rutile-brookite mixtures [23,24]. Only a small difference is observed in band gap of samples as they are practically independent of different phases [31]. The decrement in band gap values can be attributed to the difference in band alignment of each phase in a composite which significantly lower the band gap due to the difference in ionization potentials and chemical bonding of each phase [32].

### 3.4. Comparison of water splitting efficiencies of different $\text{TiO}_2$ nanotubes

The photocatalytic water splitting experiments of all the samples are carried out in water, containing ethanol as a sacrificing agent. The  $\text{H}_2$  evolution rate of  $\text{TiO}_2$  nanotubes at different time intervals are depicted in Fig. 8. The highest hydrogen evolution of 645  $\mu\text{mol/g}$  is observed for T-11, after 4 h of light irradiation. The hydrogen evolution of T-9.5 is less compared to T-10.2. This may be due to the efficient electron transport along anatase-rutile interface in T-10.2. When compared to T-10.2, the hydrogen generation is more in T-11, T-12 and T-15 samples. This is due to the presence

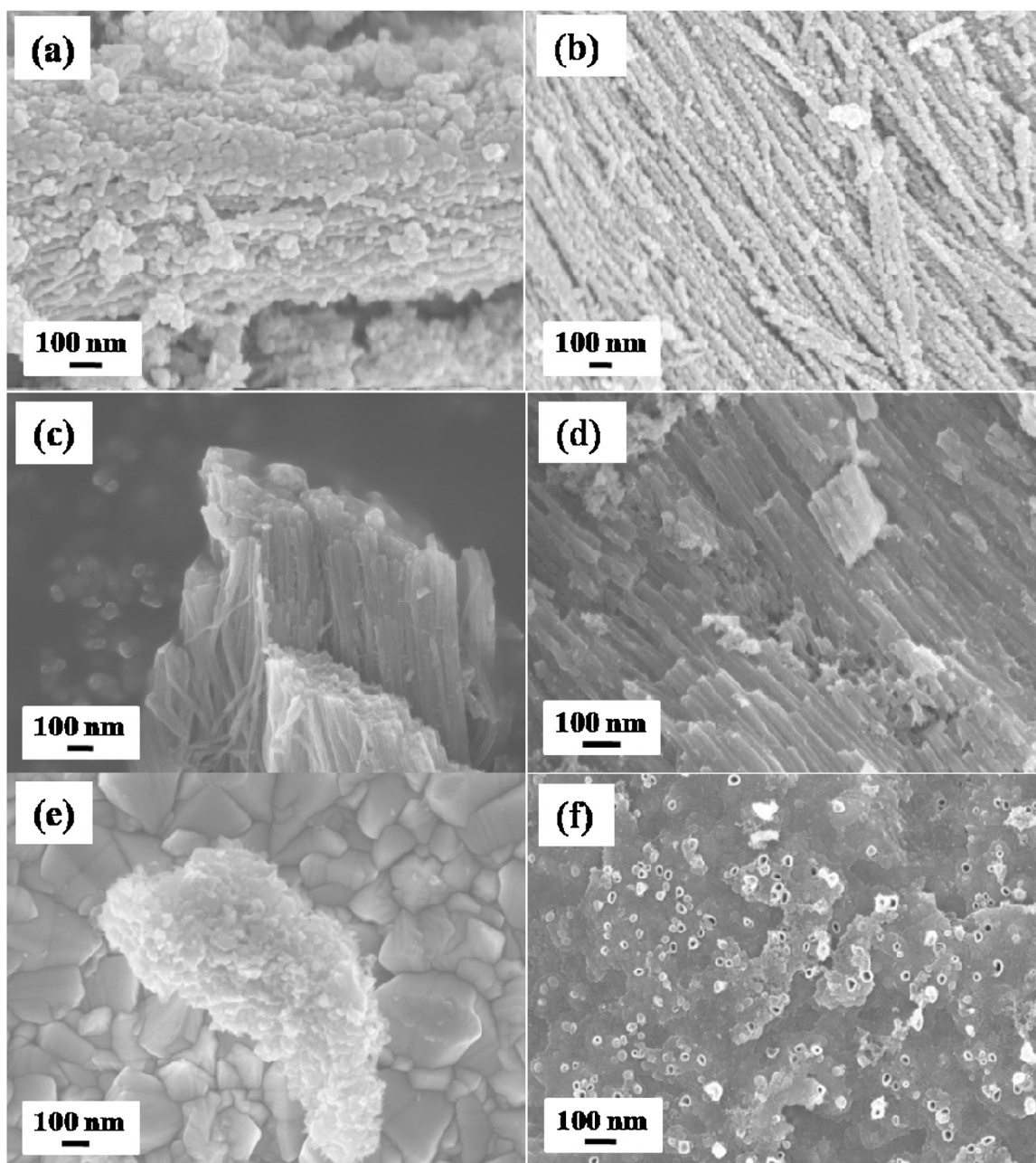


**Fig. 4.** FESEM images of (a) T-9.5, (b) T-10.2, (c) T-11, (d) T-12, (e) T-15 and (f) the perpendicular view of the T-11 nanotubes in which the tubular openings are visible.

of anatase, rutile and brookite phases in the nanotubes of T-11, T-12 and T-15, which enhances the charge separation by the facile movement of charge carriers across the interfaces. Among the triphase samples, overall hydrogen generation results show that the T-11 nanotube samples is best at its efficiency. This can be attributed to the better crystallinity of the phases in the nanotubes which enhances charge transport thereby facilitating charge separation leading to effective water splitting [19]. The high efficiency of T-11 may also be due to enhanced light absorption as evident from the observed low band gap (Fig. 7). Despite the fact that T-12 possesses similar characteristics as T-11, the noticeable difference in hydrogen generation efficiency is due to the presence of defects which is discussed later with respect to Fig. 10c. The low reactivity of T-15 can be attributed to the destruction of tubular morphology leading to reduction in active surface area for photocatalysis.

### 3.5. Mott-Schottky analysis

To ascertain the improvement in charge separation due to band alignment in triphase system compared to biphasic and single phase systems, Mott-Schottky analysis are performed under UV light for T-9.5, T-10.2, T-11 and T-12 samples in 0.5M Na<sub>2</sub>SO<sub>4</sub> electrolyte. Fig. 9 represents the Mott-Schottky plots, from which the flat potential  $E_{fb}$  is calculated using the Mott-Schottky relation [13]

$$(C_{sc})^{-2} = \frac{2(E - E_{fb} - \frac{kT}{e})}{N_D \epsilon \epsilon_0 e A^2} \quad (6)$$

Where,  $C_{sc}$  = space charge capacity,  $N_D$  = charge carrier density of the sample,  $\epsilon$  = dielectric constant of the sample (100 for TiO<sub>2</sub> nanotubes),  $\epsilon_0$  = permittivity in vacuum and  $A$  = active surface area.  $E_{fb}$



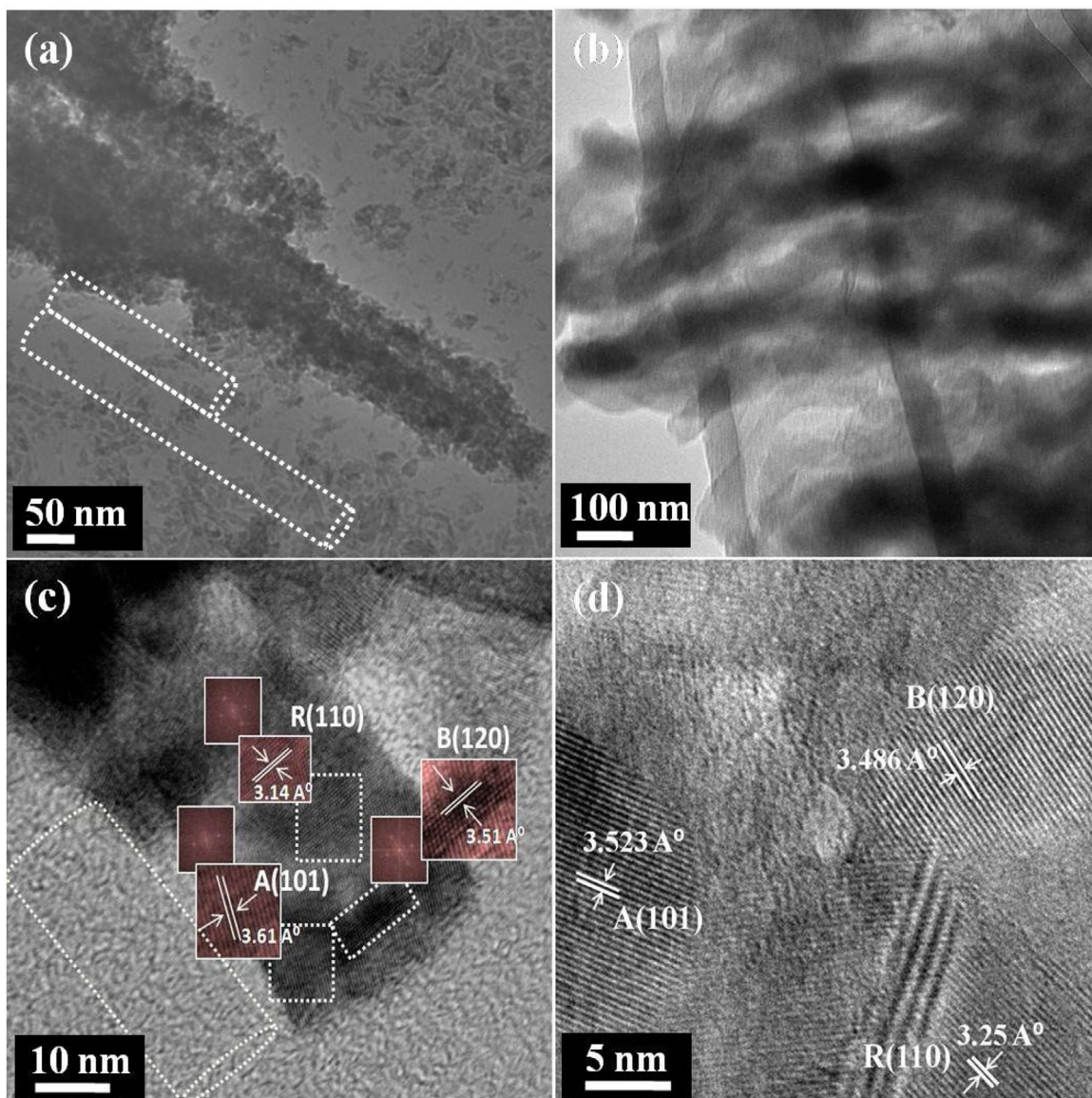


Fig. 5. (a) and (b) Bright field images of TiO<sub>2</sub> nanotubes; and (c), (d) HRTEM images of T-11.

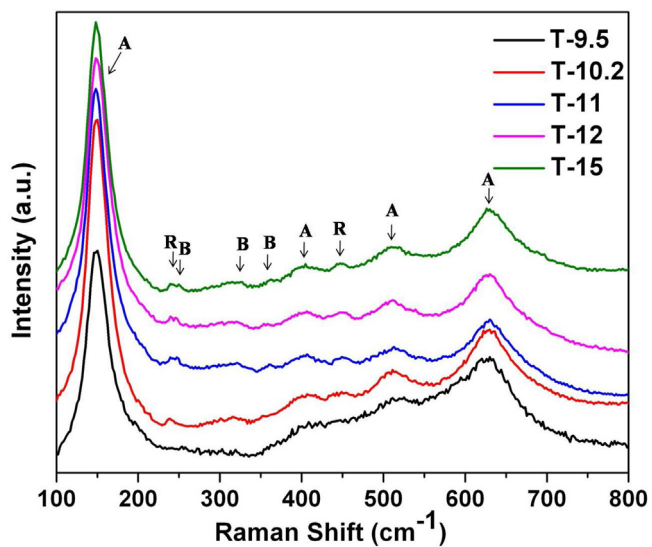


Fig. 6. Raman spectra of TiO<sub>2</sub> photocatalysts.

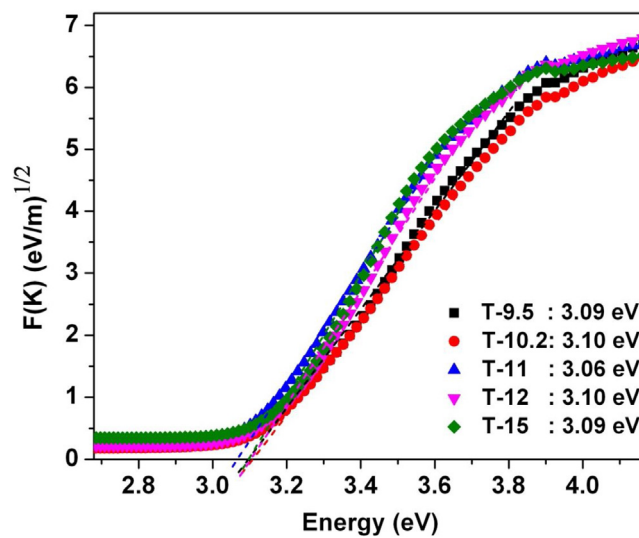
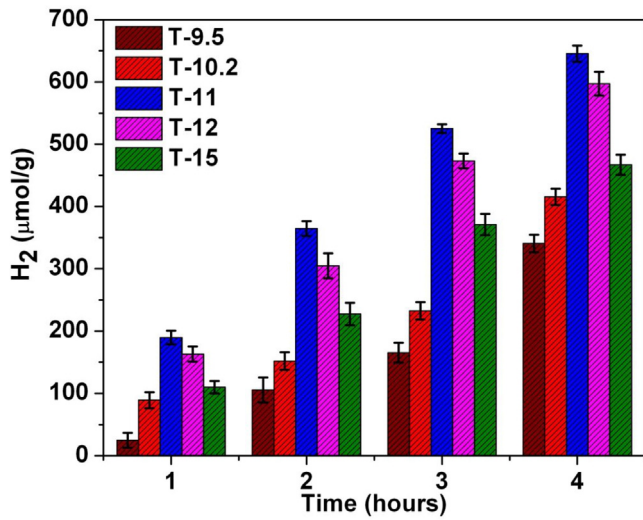
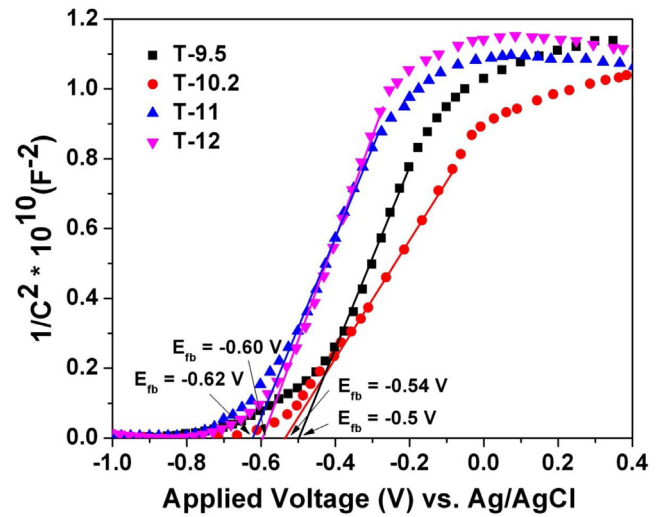


Fig. 7. Kubelka-Munk plot of TiO<sub>2</sub> polymorphs.



**Fig. 8.** Cumulative hydrogen generation of triphasic TiO<sub>2</sub> under one sun conditions with ethanol as sacrificial agent (The error bars in the figure are standard error values of three tests).



**Fig. 9.** Mott-Schotky plots of T-9.5, T-10.2, T-11 and T-12 in 0.5 M Na<sub>2</sub>SO<sub>4</sub> at a frequency of 1 KHz, under UV illumination.

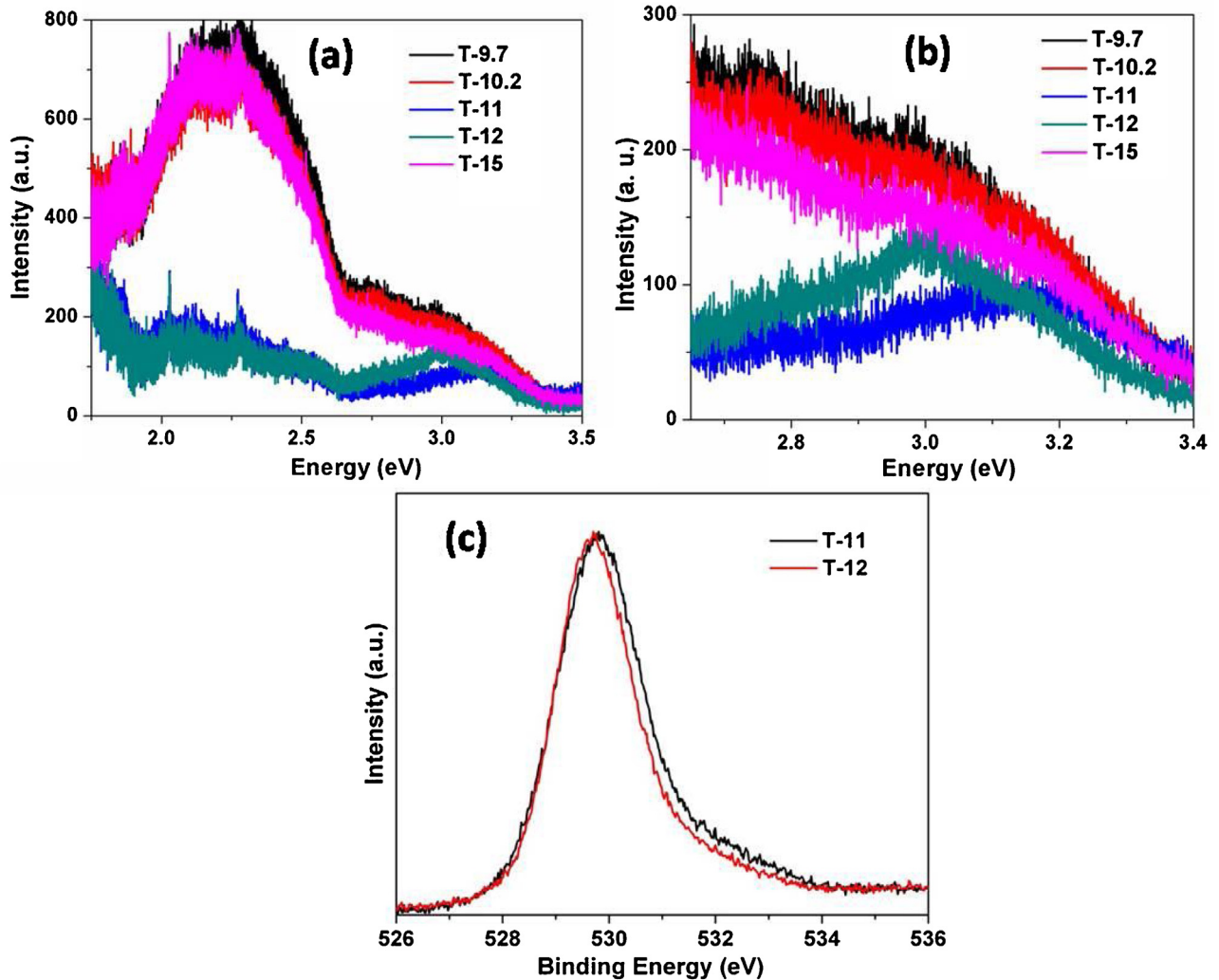


**Fig. 10.** (a) PL spectra (b) A close look of the PL spectra in band gap region from 2.6 eV to 3.4 eV and (c) O1s XPS spectra comparison of T-11 and T-12.

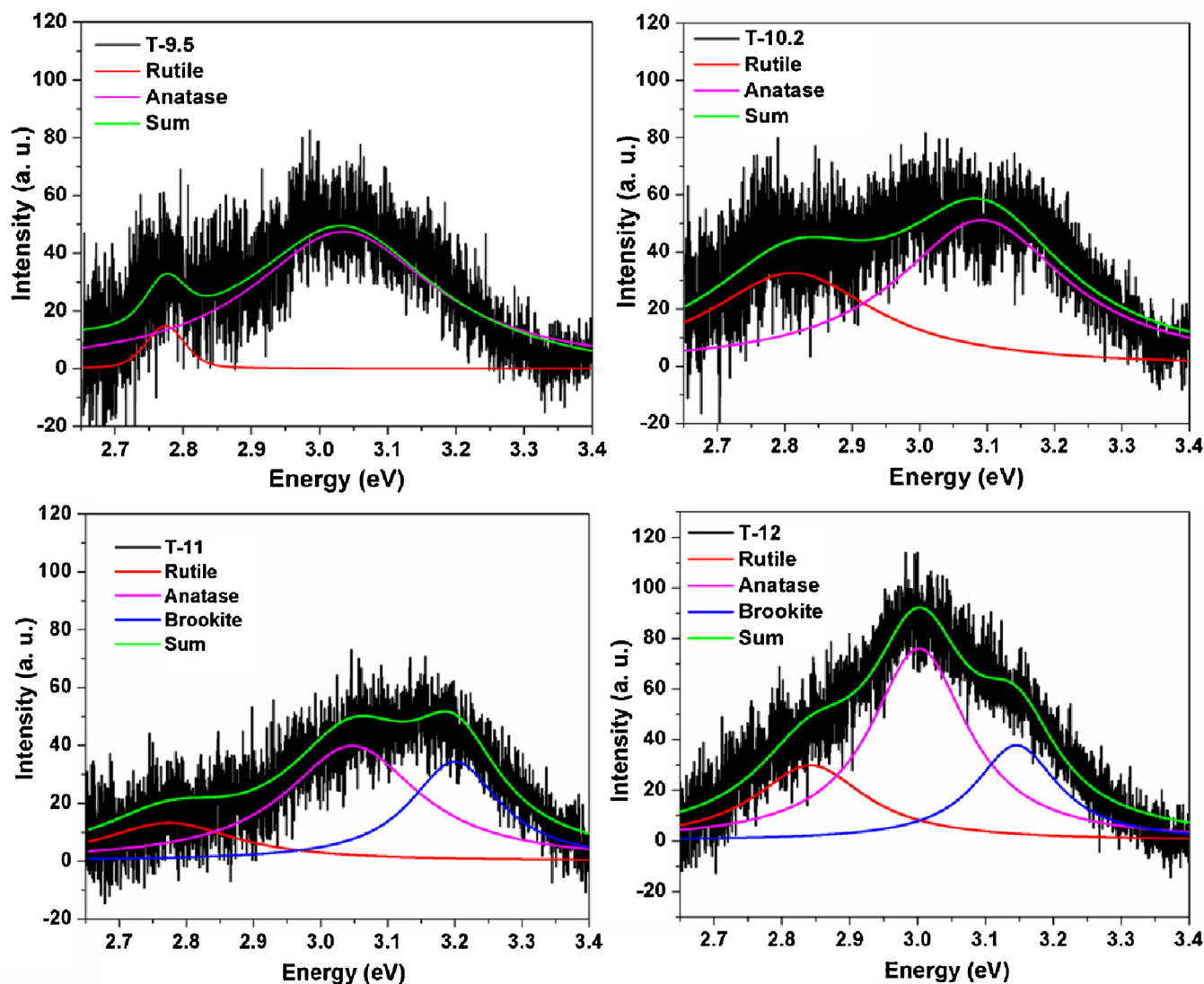


Fig. 11. Deconvoluted PL spectra in the region from 2.6 eV to 3.4 eV.

is calculated from the intercept extrapolating a straight line from  $1/C^2$  versus potential plot. The calculated  $E_{fb}$  values are given in Fig. 9.

All samples exhibit a positive slope in Mott schottky plots, as expected for n-type semiconductors. The observed cathodic shift in flat band potential is in the order of T-11 > T-12 > T-10.2 > T-9.5. When  $TiO_2$  is irradiated, the upward shift of the Fermi level enhances the charge separation at the semiconductor/electrolyte interface leading higher degree of band bending at the  $TiO_2$  surface compared to that in dark. The electrons in conduction band and holes in the valence band take part in the redox reaction [33,34]. In a multi-phase system, under UV illumination, the excited charge carriers transfer from one phase to another leading to a higher shift in the Fermi level towards the conduction band edge (as in the case of triphase (T-11 and T-12) and biphasic (T-10.2)). This causes higher degree of band bending and hence higher flat band potential. The degree of Fermi level shift depends on the number of phase junctions present. The difference in flat band potential among the different samples T-11 > T-12 > T-10.2 > T-9.5 supports that more the phase junction more the band bending (flat band potential) and hence better charge separation.

The crystallite size analysis of T-11 and T-12 titania polymorphs calculated from XRD (Fig. 3) are given in Table 2. From Table 1, it is clear that T-11 and T-12 shows comparable phase percentages.

Table 2

Crystallite Size of all the three phases in T-11 and T-12 polymorphs.

Phases	T-11 (nm)	T-12 (nm)
Anatase	6.738	6.984
Rutile	6.173	6.326
Brookite	5.195	6.195

However, crystallite size analysis indicates a marginally smaller crystallite size of anatase and rutile, and significantly smaller size of brookite in T-11 compared to T-12. This difference in crystallite size would lead to more number of bulk heterojunctions and is expected to assist in effective charge separation. This reflects in the Mott-Schottky plots presented above ( $E_{fb}$  of T-11 > T-12). Further, the presence of all three phases in close proximity in T-11, as observed in the HRTEM analysis (Fig. 5c and d), directly supports the presence of bulk heterojunctions.

### 3.6. Detailed study of PL spectra

The photoluminescence spectra (Fig. 10a and b) are analyzed to study the photophysics of the photogenerated species in the samples. In Fig. 10a, the high PL intensity is observed for T-9.5, T-10.2 and T-15 whereas the intensity is comparatively low for T-11 and



**Table 3**  
Deconvoluted peak parameters of PL spectra for different samples.

Sample	T-9.5		T-10.2		T-11		T-12	
	Centre	Area	Centre	Area	Centre	Area	Centre	Area
Peak 1	2.774	1.23	2.81	15.5	2.77	5.08	2.84	9.26
Peak 2	3.03	24.28	3.07	24.53	3.04	15.13	3.02	20.79
Peak 3	–	–	–	–	3.2	8.83	3.19	8.84

T-12 samples. In general the PL intensity in the region from 1.75 eV to 2.65 eV is due to the defects present in the sample, which act as electron traps. The peak around 2.11 eV is due to the oxygen vacancy related defects in addition to the under-coordinated Ti acting as electron traps [35,36]. The broad green emission peaked at 2.3 eV is usually assigned to the surface defects caused by oxygen deficiency and the associated  $\text{Ti}^{3+}$  ions [36–39]. It is noted that the emission intensity in 1.75 eV to 2.65 eV is quenched for T-11 and T-12. This may be due to the passivation of oxygen vacancies residing along the nanotube walls [40]. This passivation suggests the efficient transport of charge carriers along the axis of the nanotubes [40]. This is in accord with the observation of high crystallinity and good tubular morphology in T-11 and T-12 in which the three phases favors efficient transport of excitons for water splitting [19]. Compared to T-12, T-11 has relatively large intensity in this region. This may be due to the presence of excess defects in T-11. This is confirmed by XPS analysis of T-11 and T-12 samples. The O1s spectra of T-11 and T-12 are compared in Fig. 10c. It is clear that there is an excessive shoulder for T-11 which is due to the presence of excess oxygen vacancies [13]. It is well known that the presence of oxygen vacancies in  $\text{TiO}_2$  decrease the band gap. This is further confirmed by a slight decrease in band gap of T-11 compared to T-12 (Fig. 7).

The high energy emission in the region from 2.65 eV to 3.4 eV (Fig. 10b) can be either due to the self trapped excitons located at  $\text{TiO}_6$  octahedra or due to the near band edge emission. As our samples are composed of different phases, the deconvolution is necessary for the further insight. The emission spectra of T-9.5, T-10.2, T-11 and T-12 samples are deconvoluted in this region after background subtraction is represented in Fig. 11. The peak parameters such as peak centre and area are shown in Table 3. It can be seen from Table 3 and Fig. 11, that only two peaks are fitted into the spectra of T-9.5 and T-10.2, whereas three peaks are required to fit the spectra of T-11 and T-12. The strong emission appears around 3 eV which is dominant in all the samples can be attributed to the allowed indirect transition from the edge to the centre of the Brillouin zone of anatase namely  $\text{X}_{2b} \rightarrow \Gamma_{1b}$  (3.05 eV) as calculated by Daude et al. [41]. The band gap estimated from Tauc plot of T-9.5 which is majorly anatase is also calculated to be 3.05 eV. Therefore the value 3.05 eV can be considered as the band gap of anatase phase present in all the samples. The estimated band gap of anatase is lower than that of usually reported value 3.2 eV which may be due to the lack of crystallinity (in the case of T-9.5 and T-10.2) [18] and due to the presence of mixture of phases as in the case of T-11 and T-12 [31].

Our observation of the lowest energy emission around 2.8 eV in the deconvoluted PL spectra of all the samples cannot be considered as the typical energy transition  $\text{X}_{1a} \rightarrow \Gamma_{1b}$  (2.91 eV) in anatase phase proposed by Daude et al. [41] as the values are very different. It is also observed that the area of the peak around 2.8 eV is very low in T-9.5 whereas it increased nearly 12 times in T-10.2 and exists in rest of the samples with small variation in area. This leads us to an idea that the peak may be due to the near edge transition in rutile phase which in itself a direct band gap semiconductor. Therefore the low intensity of the 2.8 eV peak in T-9.5 can be attributed to the residual rutile present in the sample as already observed in XRD (Fig. 2). The red shifted rutile peak from the reported value of

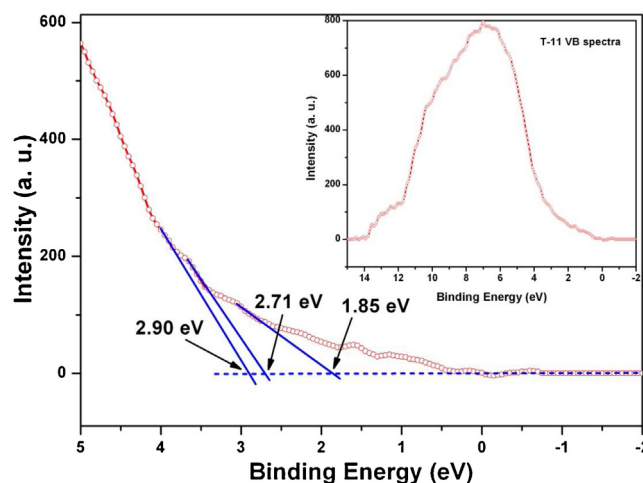


Fig. 12. Ultraviolet photoelectron valence band spectra of T-11.

2.98 eV may be because of the small crystallite size of rutile in the nanotube [42]. The peak centered at around 3.2 eV occurring in T-11 and T-12 samples can be attributed either to the band edge transition/lowest energy indirect transition in brookite phase present in the sample or due to the high energy emission of anatase due to the transition  $\Gamma_{3-} \rightarrow \text{X}_{1b}$  (3.19 eV) as proposed by Daude et al. However, it is noted that the 3.2 eV peak is absent in T-9.5 and T-10.2 where the brookite phase is absent (confirmed by XRD). Also there are many literatures in which the band gap of brookite is calculated to be in the range of 3.1–3.4 eV [24,43–47]. So it is concluded that the peak at 3.2 eV is arising from the band edge transition in brookite phase present in the sample. Thus, it can be roughly estimated from the deconvolution of the PL spectra that the band gap of anatase, rutile and brookite are around 3 eV, 2.8 eV and 3.2 eV respectively.

### 3.7. Band edge analysis of triphase $\text{TiO}_2$ and its possible charge transfer pathway

Fig. 12 shows the Ultraviolet Photoelectron Spectra (UPS) spectrum of T-11 sample after background subtraction recorded using incident photon energy of 27 eV. It can be seen that for the valence band spectra (low binding energy side, shown in the expanded view) there are three leading edges (valence band onsets) of the valence band. The density of states observed in Fig. 12 in 0–1 eV region can be attributed to occupied defects states due to partial population of Ti 3d states [48–50]. This is also evident from the O 1s core level spectra of the sample T-11 (Fig. 10c), which clearly indicates the presence of oxygen vacancy. The intersection point of the tangents to the leading edge of the valence band onset and the zero line is taken as the valence band onset point. The points of intersections of the linearly extrapolated tangents with the binding energy axis are found to be 1.85, 2.71 and 2.9 eV. However labeling these valence band edge values to the specific phases of T-11 sample is difficult as we have got a single band gap value from DRS. Hence to obtain a clear picture on the valence band edges of anatase, rutile and brookite phases in T-11, the assistance of deconvoluted PL spectra are sought. The estimated band gap values of anatase, rutile and brookite phases in T-11 from the deconvoluted PL spectra (Fig. 11c and Table 3) are 3.04, 2.77 and 3.2 eV respectively. The valence band edges obtained from the UPS analysis are 1.85, 2.71 and 2.9 eV, which are actually the energy gap between the Fermi level and the valence band maxima of the respective phases. According to the compatibility of these two sets of values, the rutile valence band edge can be fixed as 1.85 eV as the other values (2.71 and 2.90 eV) gives either near zero or negative values

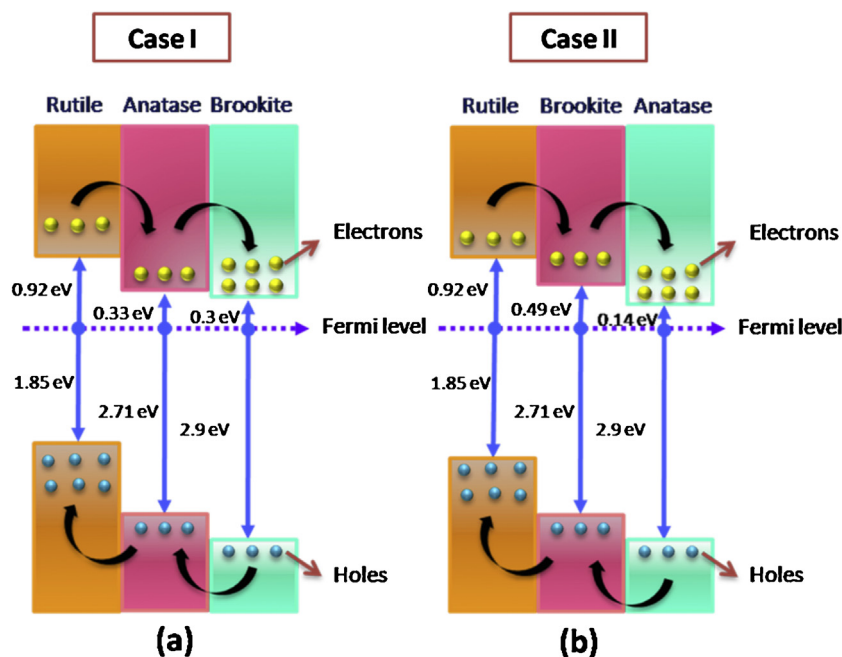


Fig. 13. Possible band edge positions of T-11 (a) Case I and (b) Case II.

when subtracted from the band gap of rutile is 2.77 eV. Therefore there are two cases to be considered to draw a band diagram of T-11. They are: case I – fixing anatase valence band edge as 2.71 eV and brookite edge as 2.9 eV and case II- fixing anatase edge as 2.9 eV and brookite edge as 2.71 eV. The band diagrams resulted out of these assumptions, are depicted in Fig. 13. The probable electron transfer pathway for case I, deduced from Fig. 13a, is rutile to anatase to brookite and the holes transfer in reverse direction. Similarly, the probable electron transfer pathway for case II based on Fig. 13b, is from rutile to brookite to anatase with hole transfer in opposite direction.

It can be seen that the gap between conduction band edge and Fermi level of anatase in case II is very less (0.14 eV) compared to that of brookite in case I (0.3 eV) from Fig. 13. For efficient hydrogen production, the conduction band edge must be more negative than the reduction potential of  $H^+$  to  $H_2$  ( $E_{H^+/H_2} = 0V$  vs. NHE at pH=0) [51]. Hence the electron transfer pathway corresponding to case I (Fig. 13a) can be considered as the probable one. The overall peak position of PL spectra (the sharp peak in the range of 2.6 eV to 3.4 eV) of T-11 (Fig. 10b) is observed at 3.14 eV which is around the band gap value of brookite. This high emission intensity around brookite can be attributed to the large recombination at brookite phase compared to anatase and rutile phases. This can happen when electrons get accumulated in brookite due to their transfer from rutile to anatase to brookite after excitation by light. A similar transfer pathway is suggested by Kaplan et al. [19] as the charge separation is enhanced by the synergistic effect of anatase and rutile as recognized by already reported literatures [13] and due to the preferential oxidation reaction at brookite phases. It is also reported by Scanlon et al. [32] that the photogenerated electrons flow from rutile to anatase due to the high electron affinity of anatase in an anatase-rutile composite whose band gap is significantly lowered. From these observations, it can be concluded that the transfer pathway of electrons in ARB system is from rutile to anatase to brookite.

The overall peak position of T-12 in Fig. 10b is at 3 eV which is close to the band gap of anatase ascertained from the deconvolution of PL spectra. This indicates the possibility of higher electron hole recombination in the anatase phase of T-12 sample. A compar-

ison of the deconvoluted PL peak areas of T-11 and T-12 samples (Table 3) reveal that the peak area corresponding to the rutile and anatase phases (around 2.8 eV and 3 eV) in T-12 is high compared to T-11; whereas, the peak area corresponding to brookite phase (around 3.2 eV) is almost equal. Therefore it is clear that the relatively high anatase rutile phase content in T-12 (Table 1) causes high charge recombination at anatase and rutile phases, which substantially decrease the rate of electron transfer to brookite leading to the low photocatalytic efficiency of T-12 compared with T-11.

#### 4. Conclusion

In summary, the present study demonstrates facile synthesis of anatase-rutile-brookite  $TiO_2$  nanotubes and its application in photocatalytic water splitting. The efficiency of triphase  $TiO_2$  in hydrogen generation is compared with anatase-rutile and anatase  $TiO_2$  nanotubes. It is found that the triphase  $TiO_2$  is more efficient than biphasic and single phase  $TiO_2$  nanotubes in photocatalytic water splitting. The transfer pathway of charge carriers in triphase  $TiO_2$  nanotubes are determined using deconvolution of PL spectra and valence band edge analysis. It is demonstrated that the excited electron transfers from rutile to anatase to brookite in triphase  $TiO_2$ .

#### Acknowledgment

Authors whole heartedly thank Dr. A.K. Sinha, Scientific Officer G, Indus Synchrotrons Utilization Division, Raja Ramana Centre for Advance Technology, Indore, India, for his guidance in Synchrotron XRD analysis.

#### References

- [1] A. Züttel, M. Hirscher, B. Panella, K. Yvon, S.-i. Orimo, B. Bogdanović, M. Felderhoff, F. Schüth, A. Borgschulte, S. Goetze, S. Suda, M.T. Kelly, Hydrogen as a Future Energy Carrier, Wiley-VCH Verlag GmbH & Co. KGaA, 2008, pp. 165–263.
- [2] N.Z. Muradov, T.N. Veziroğlu, Int. J. Hydrogen Energy 33 (2008) 6804–6839.
- [3] A. Fujishima, K. Honda, Nature 238 (1972) 37–38.
- [4] O. Khaselev, J.A. Turner, Science 280 (1998) 425–427.
- [5] A. Kudo, Y. Miseki, Chem. Soc. Rev. 38 (2009) 253–278.

- [6] K. Maeda, D. Lu, K. Teramura, K. Domen, *Energy Environ. Sci.* 3 (2010) 470–477.
- [7] O. Kiyonori, I. Akio, T. Kentaro, T. Kenji, H. Michikazu, D. Kazunari, *Chem. Lett.* 36 (2007) 854–855.
- [8] T. Luttrell, S. Halpegamage, J. Tao, A. Kramer, E. Sutter, M. Batzill, *Sci. Rep.* 4 (2014) 4043.
- [9] G. Sivalingam, K. Nagaveni, M.S. Hegde, G. Madras, *Appl. Catal. B: Environ.* 45 (2003) 23–38.
- [10] R.P. Antony, T. Mathews, C. Ramesh, N. Murugesan, A. Dasgupta, S. Dhara, S. Dash, A.K. Tyagi, *Int. J. Hydrogen Energy* 37 (2012) 8268–8276.
- [11] G. Li, K.A. Gray, *Chem. Phys.* 339 (2007) 173–187.
- [12] X. Chen, S.S. Mao, *Chem. Rev.* 107 (2007) 2891–2959.
- [13] L.K. Preethi, R.P. Antony, T. Mathews, S.C.J. Loo, L.H. Wong, S. Dash, A.K. Tyagi, *Int. J. Hydrogen Energy* 41 (2016) 5865–5877.
- [14] H. Zhao, L. Liu, J.M. Andino, Y. Li, J. Mater. Chem. A 1 (2013) 8209–8216.
- [15] B.K. Mutuma, G.N. Shao, W.D. Kim, H.T. Kim, J. Colloid Interface Sci. 442 (2015) 1–7.
- [16] H. Xu, L. Zhang, *J. Phys. Chem. C* 113 (2009) 1785–1790.
- [17] Y. Liao, W. Que, Q. Jia, Y. He, J. Zhang, P. Zhong, *J. Mater. Chem.* 22 (2012) 7937–7944.
- [18] A. Di Paola, M. Bellardita, R. Ceccato, L. Palmisano, F. Parrino, *J. Phys. Chem. C* 113 (2009) 15166–15174.
- [19] R. Kaplan, B. Erjavec, G. Dražić, J. Grdadolnik, A. Pintar, *Appl. Catal. B: Environ.* 181 (2016) 465–474.
- [20] T. Lopez, R. Gomez, E. Sanchez, F. Tzompantzi, L. Vera, *J. Sol–Gel Sci. Technol.* 22 (2001) 99–107.
- [21] F. Wei, H. Zeng, P. Cui, S. Peng, T. Cheng, *Chem. Eng. J.* 144 (2008) 119–123.
- [22] N. Mahdjoub, N. Allen, P. Kelly, V. Vishnyakov, *J. Photochem. Photobiol. A: Chem.* 210 (2010) 125–129.
- [23] A.M. Luís, M.C. Neves, M.H. Mendonça, O.C. Monteiro, *Mater. Chem. Phys.* 125 (2011) 20–25.
- [24] A. Di Paola, G. Cufalo, M. Addamo, M. Bellardita, R. Camprotrini, M. Ischia, R. Ceccato, L. Palmisano, *Colloids Surf. Physicochem. Eng. Asp.* 317 (2008) 366–376.
- [25] R.P. Antony, T. Mathews, A. Dasgupta, S. Dash, A.K. Tyagi, B. Raj, *J. Solid State Chem.* 184 (2011) 624–632.
- [26] N.F. Fahim, T. Sekino, *Chem. Mater.* 21 (2009) 1967–1979.
- [27] R. Hahn, J.M. Macak, P. Schmuki, *Electrochem. Commun.* 9 (2007) 947–952.
- [28] H. Zhang, J.F. Banfield, *J. Phys. Chem. B* 104 (2000) 3481–3487.
- [29] V. Swamy, B.C. Muddle, Q. Dai, *Appl. Phys. Lett.* 89 (2006) 163118.
- [30] B. Zhao, F. Chen, Q. Huang, J. Zhang, *Chem. Commun.* (2009) 5115–5117.
- [31] T. Torimoto, N. Nakamura, S. Ikeda, B. Ohtani, *PCCP* 4 (2002) 5910–5914.
- [32] D.O. Scanlon, C.W. Dunnill, J. Buckeridge, S.A. Shevlin, A.J. Logsdail, S.M. Woodley, C.R.A. Catlow, M.J. Powell, R.G. Palgrave, I.P. Parkin, G.W. Watson, T.W. Keal, P. Sherwood, A. Walsh, A.A. Sokol, *Nat. Mater.* 12 (2013) 798–801.
- [33] G.G. Bessegato, T.T. Guaraldo, M.V.B. Zanon, *Modern Electrochemical Methods in Nano, Surface and Corrosion Science*, in: M. Aliofkhazraei (Ed.), InTech, Rijeka, 2014 (p. Ch. 10).
- [34] G. Wang, H. Wang, Y. Ling, Y. Tang, X. Yang, R.C. Fitzmorris, C. Wang, J.Z. Zhang, Y. Li, *Nano Lett.* 11 (2011) 3026–3033.
- [35] G.C. Vásquez, M.A. Peche-Herrero, D. Maestre, A. Cremades, J. Ramírez-Castellanos, J.M. González-Calbet, J. Piqueras, *J. Phys. Chem. C* 117 (2013) 1941–1947.
- [36] C.C. Mercado, F.J. Knorr, J.L. McHale, S.M. Usmani, A.S. Ichimura, L.V. Saraf, *J. Phys. Chem. C* 116 (2012) 10796–10804.
- [37] Y. Lei, L.D. Zhang, G.W. Meng, G.H. Li, X.Y. Zhang, C.H. Liang, W. Chen, S.X. Wang, *Appl. Phys. Lett.* 78 (2001) 1125–1127.
- [38] S. Ghosh, G.G. Khan, K. Mandal, A. Samanta, P.M.G. Nambissan, *J. Phys. Chem. C* 117 (2013) 8458–8467.
- [39] A.A. Melvin, P.A. Bharad, K. Illath, M.P. Lawrence, C.S. Gopinath, *Chem. Sel.* 1 (2016) 917–923.
- [40] Z. Hongchao, Z. Min, F. Qun, L. Bo, L. Wei, G. Heshuai, W. Minghong, L. Yong, *Nanotechnology* 25 (2014) 275603.
- [41] N. Daude, C. Gout, C. Jouanin, *Phys. Rev. B* 15 (1977) 3229–3235.
- [42] H. Lin, C.P. Huang, W. Li, C. Ni, S.I. Shah, Y.-H. Tseng, *Appl. Catal. B: Environ.* 68 (2006) 1–11.
- [43] M. Grätzel, F.P. Rotzinger, *Chem. Phys. Lett.* 118 (1985) 474–477.
- [44] V. Štengl, D. Králová, *Mater. Chem. Phys.* 129 (2011) 794–801.
- [45] D. Reyes-Coronado, G. Rodríguez-Gattorno, M.E. Espinosa-Pesqueira, C. Cab, R.D. Coss, G. Oskam, *Nanotechnology* 19 (2008) 145605.
- [46] X. Shen, J. Zhang, B. Tian, M. Anpo, *J. Mater. Sci.* 47 (2012) 5743–5751.
- [47] J.-G. Li, T. Ishigaki, X. Sun, *J. Phys. Chem. C* 111 (2007) 4969–4976.
- [48] A.K. Rumaiz, B. Ali, A. Ceylan, M. Boggs, T. Beebe, S. Ismat Shah, *Solid State Commun.* 144 (2007) 334–338.
- [49] A.R. Kumarasinghe, W.R. Flavell, A.G. Thomas, A.K. Mallick, D. Tsoutsou, C. Chatwin, S. Rayner, P. Kirkham, S. Warren, S. Patel, P. Christian, P. O'Brien, M. Grätzel, R. Hengerer, *J. Chem. Phys.* 127 (2007) 114703.
- [50] C. Sánchez-Sánchez, M.G. Garnier, P. Aebi, M. Blanco-Rey, P.L. de Andres, J.A. Martín-Gago, M.F. López, *Surf. Sci.* 608 (2013) 92–96.
- [51] J. Zhu, M. Zäch, *Curr. Opin. Colloid Interface Sci.* 14 (2009) 260–269.